ELECTRONIC STRUCTURE OF MATERIALS CENTRE

Electronic Structure Investigation of Oxidized Aluminium Films with Electron Momentum Spectroscopy

X. Guo, S. Canney, A.S. Kheifets, M. Vos, Z. Fang, S. Utteridge, I.E. McCarthy and E. Weigold

ESM-140

September 1996

Electronic structure investigation of oxidized aluminum films

with electron momentum spectroscopy.

X. Guo, S. Canney, A.S. Kheifets, M. Vos, Z. Fang, S. Utteridge,

I. E. McCarthy and E. Weigold[*]

Electronic Structure of Materials Centre, The Flinders University of South Australia,

Adelaide, SA 5001, Australia

[*] Research School of Physical Sciences and Engineering, The Australian National University,

Canberra, ACT 0200 Australia

Electron momentum spectroscopy (EMS) or (e, 2e) measurements with oxidized aluminum thin films have been performed. Due to the surface sensitive nature of the EMS spectrometer employed, the measured (e, 2e) events come from the front oxidized layer as viewed by the electron detectors. The measurements show clearly two major features in the spectral momentum density distribution and they are related to the upper valence band and the lower valence band of aluminum oxide. The first is a "dual parabola" energy-momentum dispersion pattern spanning about 8 eV in the upper valence band. This "dual parabola" pattern has been qualitatively reproduced by a linear muffin-tin orbital (LMTO) calculation on spherically averaged α-Al_2O_3 with nearly the same energy span. In the lower valence band, the LMTO calculation indicates a dispersion spanning about 5 eV, and the measured spectral momentum density plot shows a similar "bowl" shape but with less dispersion. The possible causes which blur the dispersion in the lower valence band are discussed. Other features in the spectral momentum density distribution are also discussed and compared with the LMTO calculation.

I. INTRODUCTION

Electron momentum spectroscopy (EMS) is a new spectroscopic technique which can measure electron momentum distributions directly and visualize the dispersion relation between energy and momentum of electrons in solids [1] This was demonstrated by a series of (e, 2e) experiments on solid targets[2-10] in the last few years In these experiments, the new (e, 2e) spectrometer[11] of The Flinders University of South Australia was used It has increased (e, 2e) coincidence count rates (up to 1000 counts per minute[12]) and significantly improved both energy and momentum resolution. In addition to the *energy-resolved* momentum distribution of electrons in valence bands[5,8-10] and core levels[4,9] which can be uniquely measured by EMS, information has also been obtained on the influence of lattice order on the electronic structure,[6] the electronic structure of adsorbates,[7,9] and the annealing effects on the electronic structure of the surface.[3] The targets used in these investigations include carbon (amorphous carbon, graphite, highly oriented pyrolitic graphite and diamond-like amorphous carbon), semiconductors (amorphous silicon and amorphous germanium) and a semiconductor compound (polycrystalline silicon carbide). In fact EMS is now being applied to the study of a wide range of materials.

Among the wide range of materials which can be explored by EMS, metals and metal oxides are a particularly interesting group of targets. First of all, EMS on metals and metal oxides may provide a new approach to the subject of electron correlation effects which are an important factor in understanding electronic structures and properties of

solid materials from 3d metals[13] to high Tc superconductors[14]. Secondly, the interest in metals and metal oxides is not only due to their importance in fundamental aspects in solid state physics, but also due to their wide application in microelectronics. Metal oxides usually have much more complex electronic structure than metals. This provides a challenge to EMS of whether it can be applied to study materials with complex bulk structures. An interesting example is aluminum metal and aluminum oxide. Aluminum is a simple case, being a " free electron" metal with a straightforward face centred cubic (fcc) crystal structure. A parabolic free electron energy-momentum dispersion pattern should be visualized with EMS. As a matter of fact, recent EMS measurement on aluminum metal[15] showed excellent agreement with a free-electron model calculation. Aluminum oxide (Al_2O_3) is an ionic solid and an insulator and has, on the other hand, a much more complex crystal structure. In the α-Al_2O_3 form, for example, its structure may be described as a hexagonal close packing array of oxygen atoms with two-thirds of the octahedral holes occupied by aluminum atoms. Its peculiar crystal structure and wide-ranging applications have drawn both theoretical and experimental interest. Indeed, the electronic structure of aluminum oxide has been widely studied both theoretically[16-22] and experimentally.[23,24] However, there is no general agreement theoretically[17,16,19] and experimentally[23,25-29] on its band structure details, and particularly few of them have concerned the momentum distribution aspect of its valence band electrons.[24,30]

In this paper we describe our recent investigations of the electronic structure of oxidized aluminum thin films with EMS. The oxidized layers on the aluminum thin film are related to aluminum oxide (Al_2O_3). To analyze and interpret the experimental results

a spherically averaged linear muffin-tin orbital (LMTO) calculation on α-Al_2O_3 has been performed. Any of the other forms of Al_2O_3, although their band structure in the reduced zone scheme may appear completely different, are all expected to have similar momentum densities in the real momentum space.

This paper is organized as follows: the LMTO calculation on α-Al_2O_3 is described in Sec. II; Section III consists of two parts. The EMS technique and the (e, 2e) spectrometer used in this experiment are described in Sec. III-A and the details of the preparation and the characterization of the samples are given in Sec. III - B. In Sec. IV, the spectral momentum density plots of both the EMS measurement and the LMTO calculation are presented. The details of the electron energy-momentum distributions for both the upper valence band and the lower valence band are shown and discussed also in Sec. IV. Conclusions are drawn in Section V.

II. THEORY

It is known that aluminum oxide (Al_2O_3) has different structure forms such as σ-Al_2O_3, γ-Al_2O_3 and a-Al_2O_3. Even so, the broad features of their density of states and plasmon excitations are similar as indicated by X-ray photoemission spectroscopy[23] and electron energy-loss spectroscopy.[31] The XPS data of Balzarotti and Bianconi[23] also suggest that an amorphous aluminum oxide surface layer has similar electronic properties to its crystalline forms of α-Al_2O_3 and γ-Al_2O_3. For that reason it is generally accepted that α-Al_2O_3 can be taken as a suitable prototype to interpret experimental spectroscopic results.

We follow this logic and perform an *ab initio* self-consistent calculation of the electronic structure on bulk α-Al$_2$O$_3$ which we will be referring to in analysing and interpreting our experimental data. For the present calculation we employ the linear muffin-tin orbital (LMTO) method[32] in atomic sphere approximation (ASA) with von Barth and Hedin parametrization for the exchange-correlation potential[33]. Although the LMTO method is just one of many computational schemes derived within the general density functional philosophy, we find it advantageous in terms of accuracy and computational efficiency and capa¹ ᵒf performing full-scale band structure calculations on solids with a large number of valence electrons per unit cell.

The atomic arrangement in α-Al$_2$O$_3$ (corundum structure) is quite complicated. The Bravais lattice of corundum is trigonal with all the primitive lattice vectors of equal length a (9 694 a.u.) forming an equal angle β ($55^0 6'$) between any two of them[34]. In Cartesian coordinates, the primitive lattice vectors are conveniently expressed in terms of the two constants, s and r,

$$
\begin{pmatrix} t_1 \\ t_2 \\ t_3 \end{pmatrix} = \begin{pmatrix} s \cdot e_x & 0 \cdot e_y & r \cdot e_z \\ -s/2 \cdot e_x & s\sqrt{3}/2 \cdot e_y & r \cdot e_z \\ s/2 \cdot e_x & -s\sqrt{3}/2 \cdot e_y & r \cdot e_z \end{pmatrix}, \tag{1}
$$

where $s = \dfrac{2a}{\sqrt{3}} \sin(\beta/2)$ (5.17 a.u.) and $r = \sqrt{a^2 - s^2}$ (8.18 a.u.)[35] The volume of the elementary cell is $\Omega = \dfrac{3\sqrt{3}}{2} s^2 r$.

The unit cell of α-Al$_2$O$_3$ contains two molecular units of Al$_2$O$_3$ (ten atoms altogether), arranged symmetrically with respect to the origin as shown in Fig 1. The four aluminum atoms are arranged along the z-axis at distances $\pm 0.435r$ and $\pm 1.065r$[35] The two oxygen groups, each of three atoms, are arranged in two planes which are perpendicular to the z-axis and cross it at distances $\pm 0.750r$. The oxygen atoms form equilateral triangles with length of $0.574r$.

The essence of the LMTO-ASA method is that the atomic polyhedron is filled with a number of atomic spheres each of which represents a non-equivalent atomic position This method is mostly suitable for close-packed structures whose elementary cell can be spanned effectively by touching atomic spheres. "Open" structures such as the diamond one can be treated by adding "empty" atomic spheres at the interstitial sites[36] We follow this scheme for corundum and place two additional "empty" spheres at the origin and the z-axis at a distance of 1.50r. The equivalent position at a distance of -1.50r can be reached by a primitive vector translation $\sim t_1 - t_2 - t_3$ and is not included in the muffin-tin basis. So, we have $N = 12$ atomic spheres in the basis each of the radius

$$
R_s = \left(\frac{1}{N} \frac{3}{4\pi} \Omega \right)^{1/3} \approx 2.246 \text{ a.u.}
$$

The valence band structure of α-Al$_2$O$_3$ along the two high-symmetry directions, ΓX and ΓZ, is plotted in Fig. 2 together with the Brillouin zone of the α-Al$_2$O$_3$ crystal. There are total of 24 bands which accommodate 48 electrons in the elementary cell. The most characteristic feature of the valence band in Al$_2$O$_3$ is its split into two sub-bands which

are commonly labeled the lower and upper valence bands. The lower valence band (LVB) comprising 6 separate bands originates from the $2s$ states of 6 oxygen atoms. In our model the LVB spans approximately 3.4 eV. The upper valence band (UVB) comprises 18 individual bands. They are derived from the oxygen $2p$ orbitals. The UVB span is approximately 7.3 eV. The interband gap is 8.6 eV.

It is worthwhile to compare the present band structure calculation with the earlier theoretical results which are summarized in Table 1. All the calculations on α-Al_2O_3 reported to date can be classified into either *ab initio* (or first-principle calculations), or semi-empirical calculations which use a set of adjustable parameters to fit spectroscopic data available from experiment. As it is seen from the table, the semi-empirical models produce a significantly wider valence band than that from the *ab initio* calculations. This result was noted previously by Ciraci and Batra[19]. One of the possible explanations of this phenomenon is that wider bands from the spectroscopic experiments are due to the poor quality of the samples and/or insufficient energy resolution. By the very nature of the fitting procedure the semi-empirical models reproduce these bands. *Ab initio* models are free of any of the adjustable parameters and not effected by any experimental results.

We should mention that not only are our valence band widths in good agreement with other *ab initio* calculations, but also the intimate details of our band structure calculation are very close to those reported by other authors (see, for instance, Fig. 2 of Ref. 20).

After producing the valence band structure from the LMTO model we proceed with the spectral momentum density calculation. This is a quite straightforward procedure

described elsewhere.[37,38] The results of the momentum density calculation are presented in Fig. 3 for the three major high-symmetry directions ΓX, ΓY and ΓZ, and in Fig. 6 as a spherical average to be compared directly with the present experimental data.

The two-dimensional band energy and momentum density plots of Fig. 3 allow us to restore the three-dimensional spectral momentum density in the three major high-symmetry directions. The LVB disperses along an approximate parabola near the centre of the Brillouin zone (BZ). After it reaches the BZ boundary it either bends down (ΓZ direction) or remains flat (ΓX, ΓY direction). The momentum density decreases fast beyond the first BZ. So only the free parabola-like part of the dispersion curve will be observable in the experiment.

Behaviour of the UVB is quite peculiar. It disperses downwards right from the centre of the BZ. The momentum density increases and peaks near the middle of the second BZ. So, experimentally, one would observe a parabola-like shape with a minimum in energy shifted away from zero momentum.

Since in all the three directions the momentum density and the band energies are quite similar, the same pattern of the spectral momentum density will persist after spherically averaging over the irreducible wedge of the BZ. Result of this averaging is shown in Fig. 6 as a linear grey scale plot. The LVB displays itself as a "bowl" while the UVB has a peculiar form of a dual parabola-like shape in the spherically averaged spectral momentum density plot (Fig. 6, central panel). These characteristic features will be discussed later together with the experimental data.

III. EXPERIMENTAL DETAILS

A. EMS technique and the spectrometer

Electron momentum spectroscopy is based on the (e, 2e) reaction.[39] In an (e, 2e) reaction, under suitable conditions, a binary collision occurs in which a high energy incident electron with energy E_o and momentum p_o collides with one of the bound electrons in the target and the scattered (the fast one, energy E_f, momentum p_f) and ejected (the slow one, energy E_s, momentum p_s) electrons are detected in coincidence and analysed for energy and momentum. Then the binding energy ε and momentum q of the bound electron in the target *before* the collision are determined via energy and momentum conservation neglecting the recoil energy of the ion:

$$E_o - \varepsilon = E_f + E_s, \qquad (2)$$

and

$$p_o + q = p_f + p_s, \qquad (3)$$

where q is the momentum of the bound electron.

It is known[1-40] that the (e, 2e) cross section at high energy and high momentum transfer is, in the independent particle approximation, proportional to the modulus square of the bound electron momentum space wavefunction $|\phi(\varepsilon,q)|^2$, i.e., the electron spectral momentum density. In the case of a crystal target the proportionality, ignoring diffraction of the incident and outgoing electrons, may be expressed as[40]

$$\frac{d^5\sigma}{d\Omega_f d\Omega_s dE_f} = (2\pi)^4 N \frac{p_f p_s}{p_o} f_d f_{ee} |\phi(\varepsilon,q)|^2, \qquad (4)$$

where N is the number of unit cells in the crystal, f_d is a dispersion factor, which is nearly 1 in practical cases, $p_f (= |p_f|)$ and $p_s (= |p_s|)$ are fixed when varying p_f and p_s (angles) to scan q, and f_{ee} is the Mott cross section for electron-electron scattering, which is very near constant for the momentum range of interest. Thus the measurement of (e, 2e) cross sections at different kinematic conditions corresponding to different momenta q at different binding energies ε via eq (2) and eq (3) is a direct measurement of the spectral momentum density $|\phi(\varepsilon,q)|^2$ of the bound electrons in the target and this is often referred to as electron momentum spectroscopy.

For crystalline solid targets diffraction of the incident and outgoing electrons in the (e, 2e) reaction may occur. When the diffraction happens equation (4) may not generally hold. However, for disordered solid targets where long range order no longer exists equation (4) is applicable. It should be noted that EMS measures the *real* momentum of the bound electrons.

The (e, 2e) spectrometer used in this experiment has been described in detail elsewhere.[11] For clarity a brief description is given here. The spectrometer is set up in a non-coplanar asymmetric geometry and in the transmission mode. A schematic representation of the geometry is shown in Fig. 4. The incident electron energy is 20 keV plus the binding energy. The thin film sample is held vertically and positioned at an angle

of 30^0 towards the incident beam. The fast and slow electrons have energies of 18.8 keV and 1.2 keV, and are measured in coincidence with two electron analysers each measuring simultaneously a range of azimuthal angles (out of the plane) and energies at polar angles of 14^0 and 76^0 respectively. With this kinematics the momenta of the target electrons are detected nominally along the y-axis within the thin film, and the spectrometer is surface sensitive to about 2 nm of the sample on the exit side due to the mean free path in the solid of the 1.2 keV outgoing electrons. The electron analyser used for measuring the fast electrons is a hemispherical analyser with a pass energy of 100 eV; the one for the slow electrons is a toroidal analyser with a pass energy of 200 eV. The ranges of energy and azimuthal angle measured by the two analysers are from 18,790 eV to 18,810 eV and from -18^0 to $+18^0$ for the hemispherical analyser, and from 1,182 eV to 1,218 eV and from $\pi-6^0$ to $\pi+6^0$ for the toroidal analyser respectively. The energy resolution has recently been improved with a monochromator incorporated with the electron gun [41] An overall measurable energy range of 56 eV with a resolution of 0.9 eV and momentum range from -3.5 to 3.5 a.u. with a resolution of 0.15 a.u. have been achieved

An *in situ* electron energy loss measurement can be easily conducted with the spectrometer by adjusting the incident electron energy to match the setting of the hemispherical analyser which views the electrons scattered into the polar angle of 14^0. Transmission electron diffraction (TED) patterns of the samples can be also measured *in situ* with a TED system attached to the spectrometer chamber.

B. Preparation and characterization of the samples

Two samples, one a self-supporting aluminum film and the other an evaporated aluminum film on an amorphous carbon substrate, were prepared for this experiment.

The self-supporting sample preparation process started with nominally 40 nm thick aluminum films, which were vacuum evaporated on rocksalt (NaCl). The aluminum film on rocksalt was cleaved to a 4×4 mm square and then slid into an 80% de-ionized water and 20% methanol solution. The aluminum film was floated off the rocksalt support and then caught with a molybdenum sample holder. The aluminum film covered a few holes (0.7 mm in diameter) of the sample holder. The sample holder was put into an oven and heated slowly to 100 ^{0}C for about one hour to evaporate the water before putting it into an ion beam sputtering vacuum chamber for further processing. The 40 nm aluminum film is too thick to be used as a target in our (e, 2e) spectrometer. Ion Beam Thinning (IBT) was therefore used to prepare the thin film to a thickness which gives a sufficient (e, 2e) coincidence count rate. This was done in the ion beam sputtering chamber with a background pressure in the low 10^{-6} Torr range. A saddle-field ion source was used to produce a well focussed Ar ion beam. At 5 kV anode voltage a 5 microamp Ar beam was produced when pure Ar gas was fed into the ion source to a pressure of 4×10^{-5} Torr. The sputter thinning took about 10 minutes. During the thinning process, a light was put underneath the film. The change of color of the film as seen from an optical microscope indicated when sufficient thinning had taken place. After the thinning process the chamber was pumped back to the base pressure and the sample was transferred under vacuum to a preparation chamber, which was in ultra high vacuum (UHV), and then to

the spectrometer chamber under UHV. An (e, 2e) coincidence count rate of 35 counts per minute was achieved. The estimated thickness of this self-supporting sample was about 15 nm.

It is known that aluminum oxidizes readily in air to form a saturated oxide layer with a thickness of about 1.5 to 2 nm[42,43] that resists further corrosion, known as passivation. Due to the reactive nature of the aluminum metal and the vacuum condition for ion sputtering in this experiment, an aluminum oxide layer remained on the aluminum film after the ion beam thinning. An Auger spectrometer, which has since been upgraded, was available in the UHV preparation chamber and was then used to characterise the aluminum film surface which was viewed by the two analysers of the spectrometer. The measured Auger electron spectrum showed a peak at 54 ± 2 eV. This peak was thought to be the $L_{\Pi\Pi\Pi}VV$ cross-transition between aluminum and oxygen in aluminum oxide (Al_2O_3), corresponding to a vacancy in the $L_{\Pi\Pi}$ level of aluminum in Al_2O_3 and cross transitions from oxygen supplying the down (recombination) and up (Auger emission) electrons as explained by Quinto and Robertson.[44] The Auger LMM peak of pure aluminum should be at 70 eV. An oxygen peak at 518 ± 2 eV was clearly observed and most likely related to the aluminum oxide layer on the aluminum film. A carbon peak at 275 ± 2 eV was also observed. This carbon contamination might come from the process of vacuum evaporation of the film or the ion beam sputtering due to the modest vacuum in the sputtering chamber, or both.

A transmission electron diffraction (TED) measurement of this sample was also performed at 10, 20 and 30 keV incident electron energies. The diffraction rings

manifested polycrystalline bulk structure of the sample and matched those of aluminum metal. Based on these measurements, we regarded this self-supporting sample as a thin film with aluminum oxide layers of thickness of $1.5 \sim 2$ nm sandwiching a polycrystalline aluminum metal film. The measured (e, 2e) events come essentially only from the oxide layer viewed by the two analysers because of the surface sensitive nature of the spectrometer

The possibility of contamination of the self-supporting sample due to the modest vacuum condition in the preparation process concerned us and we therefore prepared another sample in a different way. This sample was prepared by first evaporating 3 nm of pure aluminum on a 5 nm thick amorphous carbon film which covered the 1.0 mm diameter holes of a sample holder. The evaporation thickness was monitored with a crystal thickness monitor. The background pressure of the preparation chamber was in the lower 10^{-10} Torr range. The pressure went up to the high 10^{-9} Torr range during evaporation. The sample obtained in this way was then exposed to pure O_2 (99.9%) at 1 atm. for 2 minutes. This produced an oxidized layer with thickness of about 1.5 nm After an EMS measurement, which showed both aluminum and aluminum oxide features, this sample was covered with additional 1 nm of aluminum by evaporation and exposed to pure O_2 again at 1 atm. for 2 minutes. The reason for the second evaporation and exposure of the sample to O_2 is that the mean free path of the 1.2 keV outgoing electrons for aluminum oxide may be larger than 1.5 nm, that means that (e, 2e) events occurring beyond the 1.5 nm oxidized layer are still detectable. The oxidized layer resists further oxidation to deeper depth.

The sample front surface which would be viewed by the two analysers was characterized before and after the O_2 exposures with our newly installed Auger electron spectrometer (PHI Model 3017, Physical Electronics, Inc.) which has an energy resolution of 0.6%. The oxidized aluminum layer was clearly identified by the shift of the Auger LMM peak of the evaporated aluminum as shown in Fig. 5(a) and (b) where Fig. 5(a) is an enlarged portion of Fig. 5(c) in kinetic energy range 40 - 80 eV and Fig. 5(b) is that of Fig. 5 (d) in the same kinetic energy range. The Auger LMM peak of the pure aluminum sample was located at 69 eV (Fig. 5(a).). After the oxidation this peak shifted to 57 eV (Fig. 5(b).), indicating the formation of the aluminum oxide (Al_2O_3) layer on the surface. The carbon and oxygen peaks were still observable for the evaporated aluminum sample (Fig. 5(c)), but quite weak. An (e, 2e) count rate of 65 counts per minute with this carbon-film-supported aluminum oxide sample was obtained.

After the EMS measurement, electron energy loss spectra were measured for both of the samples at 18.8 keV incident electron energy. The spectrum for the self-supporting sample showed a sharp aluminum plasmon peak at 15 eV characterising the bulk of the sample. The aluminum double plasmon peak could be hardly seen, which indicated the sample was very thin. For the carbon-film-supported sample the spectrum showed both the sharp aluminum plasmon peak at 15 eV and the broad carbon plasmon feature at 24 eV. The electron energy loss measurement with 18.8 keV incident electron energy is not sensitive to the surface layer of the samples. The features in the electron energy loss spectra were taken into account in the procedure of deconvolution for the plasmon

excitations by the incident and outgoing electrons. The effect of the plasmon excitations on the measured spectral momentum densities will be discussed in the next section.

IV. RESULTS AND DISCUSSION

Fig. 6 presents the spectral momentum density plots as measured with the spectrometer for the aluminum oxide samples (left panel for the self-supporting sample, right panel for the carbon-film-supported sample) and calculated using the LMTO method on a spherically averaged α-Al_2O_3 (central panel) respectively. A spectral momentum density plot is an intensity distribution in an energy-momentum plane. The intensity is represented by the linear grey scale, the darker scale corresponding to a higher intensity. The highest density in all these plots has been normalized to unity for ease of comparison. The statistical uncertainties in the measured data can be gauged from the plots shown in Fig. 8 - 10. The LMTO calculation of spectral momentum density of a spherically averaged α-Al_2O_3 shown in Fig. 6 has been convoluted with the 1 eV energy resolution of the spectrometer. Because of the small mean free path of the slow electron in the solid, the (e, 2e) events can be regarded as originating almost conclusively from the aluminum oxide layer. Contributions from the aluminum metal are indeed negligible. This is clear from the measured spectral momentum densities (Fig. 6, left and right panels) where there is no obvious parabolic dispersion feature of free electrons in aluminum as measured by Canney et al[15] with the same EMS spectrometer.

As discussed earlier aluminum oxide has two distinct features in its valence band structure namely an upper valence band and a lower valence band. A previous (e, 2e)

experiment[24] on an aluminum-aluminum oxide thin foil with an energy resolution of 4.5 eV reported dispersionless structures in both the upper and lower valence bands. This is manifestly not the case in the present measurements. The present measured spectral momentum density plot shows a "dual parabola" dispersion pattern spanning about 8 eV in the upper valence band (Fig. 6, left and right panels). The LMTO calculation shows a similar "dual parabola" dispersion pattern with nearly the same energy span. Near zero momentum both the EMS measurement and the LMTO calculation exhibit lower intensity throughout the upper valence band.

There is a gap between the upper valence band and the lower valence band. The EMS measurement and the LMTO calculation give nearly the same gap. In the lower valence band, the LMTO calculation, after convolution with the energy resolution of the spectrometer, indicates a dispersion of about 5 eV. The EMS measurement shows a similar "bowl" shape in the spectral momentum density, i.e., the full width of the band becoming narrower with increasing binding energy in the lower valence band, but with less dispersion. The possible causes which blur the dispersion in the lower valence band will be discussed later. Nevertheless, one can see that the measured major features in the valence band of aluminum oxide are qualitatively reproduced by the LMTO calculation.

Actually, the two distinct features in the valence band of aluminum oxide can be explained in terms of the electronic structure of its molecular unit Al_2O_3. Aluminum oxide is an ionic solid. Its molecular unit Al_2O_3 is formed stably when each of the two aluminum atoms loses three electrons from their outermost orbitals $(3s^2, 3p^1)$ to become cation Al^{3+} and each of the three oxygen atoms gains two electrons to become anion O^{2-}.

The cation Al^{3+} and anion O^{2-} thus have the same closed shell: $1s^2 2s^2 2p^6$, i.e., the neon electron configuration. The outermost obitals of Al_2O_3 will be occupied then by $2s$ and $2p$ electrons from the oxygen atom as the aluminum atom has a larger nuclear charge than oxygen, that localizes the aluminum $2s$ and $2p$ to much greater levels (about 95 eV and 50 eV above the oxygen $2s$ level in binding energy respectively). Therefore the upper valence band of aluminum oxide is dominated by the oxygen $2p$ orbitals characterized by the maximum intensity away from the zero momentum, and the lower valence band by the oxygen $2s$ orbitals characterized by the maximum intensity at zero momentum. Admixture (or hybridization) of the aluminum electron orbitals ($3s$, $3p$) with the dominant oxygen $2p$ orbitals, and with the dominant oxygen $2s$ orbitals results in the dispersions respectively in the upper valence band appearing as a "dual parabola" and in the lower valence band as a "bowl" centered about zero momentum in the spectral momentum density plot. Similar understanding may also apply to other ionic metal and semiconductor oxides even if they have totally different crystal structures.

Before comparing the measured and the calculated spectral momentum densities in detail, let us first look at the momentum integrated binding energy spectra for the aluminum oxide samples. Fig. 7 shows the measured binding energy spectra linearly summed over momentum from -2.5 a.u. to 2.5 a.u. The data points with the error bars are the raw data for the self-supporting and carbon-film-supported samples as indicated in the legend within the figure. The raw data of the self-supporting sample have smaller intensity in the higher binding energy peak (the lower valence band) due to the absence of the carbon plasmon energy loss contributions. The solid curve represents the summed

binding energy spectrum after applying an empirical deconvolution procedure to the raw data of the carbon-film-supported sample.

The deconvolution is used to subtract the (e, 2e) events in which one of the incident or outgoing electrons has lost energy due to plasmon excitation. If one of the (e, 2e) electrons suffered energy loss due to the plasmon excitation or other inelastic processes we would get a spectral momentum density plot with a blurred shadow (excess intensity) of the valence bands in the higher binding energy region. This can be explained using the energy conservation eq. (2). If one of the outgoing electrons (say the slow one) suffered energy loss the measured electron energy would be E_s' instead of E_s, and $E_s' < E_s$, the measured binding energy $\varepsilon' = E_0 - E_s' - E_f$, i.e., $\varepsilon' > \varepsilon$. This (e, 2e) event will still have the correct timing and be included in the timing window, but the binding energy will be shifted to the higher binding energy region. To subtract the contribution of such events accurately through a deconvolution procedure, one needs the real profile of the electron energy loss $\Delta E = E_s - E_s'$. An approximate profile of the energy loss can be obtained either using Monte Carlo simulations of the (e, 2e) collision or using a response function based on electron energy loss measurements of the same material. The latter was used in the deconvolution procedure in this work. In this deconvolution procedure the energy loss features of amorphous aluminum oxide (Al_2O_3) as measured by Swanson[31], together with the main features shown in the measured energy loss spectrum for the carbon-film-supported sample were taken into account. The parameters related to the energy loss features were adjusted in the empirical deconvolution procedure to get a reasonable result.

After the deconvolution the intensity between the two main peaks corresponding to the upper and lower valence bands dropped close to zero (Fig. 7). There is a clear gap of 6.5 eV between the upper valence band and the lower valence band. This compares very well with the gap of 6.6 eV in the LMTO calculation after one convolutes the calculation with the energy resolution of the spectrometer.

A LMTO calculation of momentum integrated binding energy spectrum of α-Al_2O_3 is also shown in Fig. 7. It has been normalized so that the peak heights of the lower valence bands of the calculation and the measurement (after deconvolution) are the same. Compared to the LMTO calculation, the measured upper valence band has a broader band structure and the measured intensity is much larger than the calculated one with the present arbitrary normalization of the two. In the lower valence band the measurement shows extended tail structure in the 30 ~ 35 eV binding energy region, whereas the LMTO calculation shows a total width of 5 eV consisting of two peaks at around 26.5 eV and 29 eV and no structure at all beyond 31 eV. To further compare the measurement and the LMTO calculation and discuss these differences we need to examine the spectral momentum densities in detail. In the following discussion only the results obtained with the carbon-film-supported sample are presented and discussed as they have better statistics and show improved contrast in comparison with the self-supporting aluminum sample.

Fig. 8 shows the raw and deconvoluted data as a function of the binding energy for momentum from 0 a.u. to +1.6 a.u. at equal intervals of 0.1 a.u., together with the corresponding LMTO calculations. Due to symmetry about the momentum axis, the

positive and negative momentum bins have been summed to improve the statistics. It can be seen that the intensity of the upper valence band is fairly constant before decreasing slowly at quite high momenta. The variation of the intensity of the upper valence band with the momentum does not agree well with the LMTO calculation. The calculation contains a major contribution from the oxygen $2p$ orbital to the upper valence band. This predicts zero intensity at zero momentum with the maximum in the density at around 1 a.u. of momentum (see also Fig. 3 and Fig. 6). At all momenta the measured intensity is broader and higher than that predicted.

The deconvoluted momentum distributions at selected binding energies are presented in Fig. 9 for the upper valence band region. The spherically averaged LMTO calculations are also shown in this figure. The calculated peaks move symmetrically towards lower momentum as the binding energy increases from 10 to 18 eV, with a second peak, symmetric about zero momentum growing in intensity with increasing binding energy from 12 to 16 eV moving out from close to zero momentum, and joining the other lobe of the parabola at 16 eV. This can be seen by taking constant energy cuts through the central panel of Fig. 6, i.e., it reflects the cuts through the "dual parabola" dispersion pattern for this upper valence band structure. In the lower binding energy region of this band the oxygen $2p$ orbital character is largely responsible for the momentum distribution which is peaked at higher momenta. Moving to increasing binding energy the aluminum $3p$, $3s$ and oxygen $2p$ orbitals hybridize and create a considerable dispersion. With increasing binding energy, the contribution from aluminum $3p$ decreases whereas the contribution from aluminum $3s$ increases in the orbital hybridization. This leads to the

peaks in the momentum distribution moving to lower momentum with increasing binding energy as illustrated in Fig. 9. This is reflected in the edge of the measured momentum distribution moving towards lower momenta as the binding energy increases. However, a quantitative comparison with the LMTO calculation shows that the measured spectra have much larger intensity between the peaks at all energies shown in Fig. 9. Similarly the peaks in Fig. 8 are much broader in energy than the calculated ones at all momenta.

There are a few possible causes for these differences. First, it should be caused by multiple elastic scattering of any of the electrons. As mentioned in Sec. III-A, the EMS spectrometer measures the momenta of the target electrons along the y-axis (see Fig. 4). These momenta are determined by eq. (3) by accurately measuring the azimuthal angles (ϕ_s and ϕ_f in Fig. 4) of the outgoing electrons at fixed polar angles (76° cone and 14° cone in Fig. 4). Occurrence of multiple elastic scattering distorts the incident and outgoing directions of the electrons. As a result, it distorts the measured momentum distribution of the target electrons. This has been noticed in (e, 2e) measurements of other materials, like amorphous silicon[5], amorphous germanium[9] and polycrystalline silicon carbide.[10] There also is in these cases a significant intensity near zero momentum in the low binding energy region of the valence bands where the corresponding LMTO calculations indicate zero or negligible intensity. A detailed account of multiple elastic scattering has been given by Vos and Bottema.[45] The pronounced difference near zero momentum in the upper valence band (Fig. 9) between the calculation and the experiment could also be caused by defects which may exist in the near surface region in the samples. We know that only (e, 2e) events occurring in the near surface region are

detectable with this EMS spectrometer. The existence of these defects may affect the momentum distribution in the near zero momentum region due to charge redistribution near the defect site. Similarly, aluminum-oxygen bonds at the surface may be quite different from those in bulk.[19] Contributions from multiple elastic scattering and any local disorders are not included in our present LMTO calculation. The quantitative comparison of the measurements with the theory is hindered by the multiple scattering processes. Monte Carlo simulations of (e, 2e) collision in solids in which all possible scattering processes are included may provide a better comparison.

Now let us turn to the lower valence band region. In contrast to the upper valence band, the intensity of the lower valence band in the binding energy spectra (Fig. 8) drops significantly with increasing momentum. To examine the character of the lower valence band, the momentum distributions at different binding energies together with the LMTO calculations are presented in Fig. 10. As in Fig. 9 the deconvoluted experimental data are used in Fig. 10. The momentum distribution in Fig. 10 peaks at zero momentum at 29 eV binding energy. This is not surprising since the lower valence band is dominated by the oxygen 2s orbital. However, due to small aluminum 3p orbital contribution to the bonding combination of aluminum 3s and oxygen 2s orbitals the LMTO calculation, convoluted with the energy resolution of the spectrometer, indicates a dispersion of about 5 eV in the lower valence band. As mentioned above, the measured spectral momentum density shows less dispersion than the calculated one. The discrepancy in the dispersion between the measurement and the LMTO calculation may be in part due to excess oxygen adsorbed on the saturated aluminum oxide surface. Nevertheless, the

"bowl" shaped spectral momentum distribution is clearly seen in Fig. 6 (left and right panels) in the lower valence band and is similar in shape to that of the LMTO calculation (Fig. 6, central panel). The features of the adsorbates[7] do not completely obliterate the dispersion features of the aluminium oxide, but may smear it somewhat and consequently make a shallow (less dispersion) "bowl" in the lower valence band in the spectral momentum density plot. An experiment with controlled aluminum oxidation on aluminum may provide better understanding of this discrepancy.

One may also notice in Fig. 8 that the measured main peak in the lower valence band shows a full width at half maximum (FWHM) of about 4.5 eV at all momenta selected within an interval of 0.1 a.u., whereas the LMTO calculation shows the lower valence band with a FWHM of 1.5 eV even after one convolutes the calculation with the 1 eV energy resolution of the spectrometer. This energy width difference may be due to the amorphous nature of the sample which has not been sufficiently described by the calculation.

The intensity of the lower valence band does not appear to drop as fast with increasing binding energy as that of the upper valence band. There is a tail structure in the 30 ~ 35 eV binding energy region (Fig. 8). This tail structure can not be removed by the deconvolution without creating negative intensity in the region above the upper valence band (> 18 eV binding energy). Also, the momentum distribution in the 30 ~ 35 eV binding energy region (Fig. 10) is more similar to the 26 ~ 29 eV binding energy region rather than the 10 ~ 17 eV (the upper valence band) region. These arguments lead us to associate this tail structure with the lower valence band. Similar structures at higher

binding energies of the deepest valence level are observed in the case of noble gases, where the satellite structures of valence levels in EMS binding spectra are identified by examing their momentum distributions and allocated to corresponding symmetry manifolds [1] Indeed, if one normalizes the theoretical and the experimental lower valence band features including the tail structure in Fig. 8 to equal area rather than equal height, agreement in the upper valence band region between the experiment and the calculation improves A clear interpretation of the tail structure in the lower valence band may need theoretical calculations in which electron correlation is included.

V. CONCLUSIONS

In conclusion, the visualization of the spectral momentum density of materials with complex bulk structures using EMS has been demonstrated by performing measurements with oxidized aluminum films which are prepared in two different ways. The oxidized layers on the aluminum films are related to aluminum oxide (Al_2O_3). The measured two major features in the spectral momentum density, which are related to the upper and lower valence bands of aluminum oxide respectively, are represented qualitatively by the LMTO calculation on a spherically averaged α-Al_2O_3. In particular, the observed energy-momentum dispersion pattern spanning about 8 eV in the upper valence band is reproduced by the LMTO calculation with nearly the same energy span. In the lower valence band, the LMTO calculation indicates a dispersion of about 5 eV with maximum intensity at zero momentum. The measurement shows a similar "bowl" shape in the

spectral momentum density plot but with less dispersion and a greater band width Further EMS measurements on aluminum with controlled oxidation are in progress.

References

[1] I.E. McCarthy and E. Weigold, Rep. Prog. Phys. 54, 789 (1991).

[2] E. Weigold, Y.Q. Cai, S.A. Canney, A.S. Kheifets, I.E. McCarthy, P. Storer

and M. Vos, Aust. J. Phys. 49, 543 (1996).

[3] P. Storer, Y.Q. Cai, S.A. Canney, S.A.C. Clark, A.S. Kheifets,

I.E. McCarthy, S. Utteridge, M. Vos and E. Weigold, J. Phys. D 28, 2340

(1995).

[4] R.S. Caprari, S.A.C. Clark, I.E. McCarthy, P.J. Storer, M. Vos and

E. Weigold, Phys. Rev. B 50, 12078 (1994).

[5] M. Vos, P. Storer, Y.Q. Cai, A.S. Kheifets, I.E. McCarthy and E. Weigold,

J. Phys. Condens. Matter 7, 279 (1995).

[6] M. Vos, P. Storer, Y.Q. Cai, I.E. McCarthy and E. Weigold, Phys. Rev.

B51, 1866 (1995).

[7] M. Vos, S.A. Canney, P. Storer, I.E. McCarthy and E. Weigold, Surf. Sci.

327, 387 (1995).

[8] A.S. Kheifets, J. Lower, K.J. Nygaard, S. Utteridge, M. Vos and

E. Weigold, Phys. Rev. B 49, 2113 (1994).

[9] Y.Q. Cai, P. Storer, A.S. Kheifets, I.E. McCarthy and E. Weigold,

Surf. Sci., 334, 276 (1995)

[10] Y.Q. Cai, M. Vos, P. Storer, A.S. Kheifets, I.E. McCarthy and E. Weigold,

Phys. Rev. B 51, 3449 (1995).

[11] P. Storer, R.S. Caprari, S.A.C. Clark, M.Vos and E.Weigold, Rev. Sci.

Instrum. 65, 2214 (1994).

[12] M. Vos, R.S. Caprari, P. Storer, I.E. McCarthy and E. Weigold, Can. J.

Phys., to be published.

[13] G. van der Laan, M. Surman, M.A. Hoyland, C.F.J. Flipse, B.T. Thole,

Y.Seino, H. Ogasawara and A. Kotani, Phys. Rev. B 46, 9336 (1992)

[14] S.G. Ovchinnikov, Phys. Rev. 49, 9891(1994).

[15] S. Canney, M. Vos, A. S. Kheifets, N. Clisby, I. E. McCarthy and E. Weigold, J.

Phys.: Condens. Matter (submitted).

[16] T.J. Godin and John P. LaFemina, Phys. Rev. , B 49, 7691 (1994).

[17] Y. Xu and W.Y. Ching, Phys. Rev. B 43, 4461 (1991).

[18] M.Causa, R. Dovesi, C. Roetti, E. Kotomin, and V.R. Saunders, Chem.

Phys. Lett. 140, 120 (1987).

[19] S. Ciraci and I. P. Batra, Phys. Rev. B 28, 982 (1983).

[20] I.P. Batra, J. Phys. C 15, 5399 (1982).

[21] R.A. Evarestov, A.N. Ermoshkin and V.A. Lovchenkov, Phys. Status Solidi

B 99, 387 (1980).

[22] M.H. Reily, J. Phys. Chem. Solids 31, 1041 (1970).

[23] A. Balzarotti and A. Bianconi, Phys. Stat. Sol. (b) 76, 689 (1976).

[24] P. Hayes, M.A. Bennett, J. Flexman and J.F. Williams, Phys. Rev. B 38,

13371 (1988).

[25] G. Drager and J.A. Leiro, Phys. Rev. B **41**, 12919 (1990).

[26] C.G. Dodd and G.L. Glen, J. Appl. Phys., **39**, 5377(1968).

[27] D.W. Fischer, Adv. X-ray Anal. **13**, 159 (1970)

[28] S.P. Kowalczyk, F.R. McFeely, L. Ley, V.T. Gritsyna and D.A. Shirley, Solid State Commun. **23**, 161 (1977).

[29] I.A. Brytov and Yu. N. Romashchenko, Sov. Phys.: Solid State, **20**, 384 (1978).

[30] N.M. Persiantseva, N.A. Krasil'nikova and V.G. Neudachin, Sov. Phys. JETP **49**, 530 (1979).

[31] N. Swanson, Phys. Rev. **165**, 1067 (1968).

[32] H.L. Skriver, *The LMTO method* (Springer-Verlag, Berlin, 1984).

[33] U. von Barth and L. Hedin, J. Phys. C **5**, 1629 (1972).

[34] R. Wyckoff, *Crystal Structures* (Interscience Publishers, New Yourk, 1963).

[35] J.C. Slater, *Quantum Theory of Molecules and Solids* (McGraw-Hill, New York, 1965).

[36] D. Glötzel, R. Segall and O.K. Andersen, Solid State Comm. **36**, 403 (1980).

[37] A.S. Kheifets and Y.Q. Cai, J. Phys. C **7**, 1821 (1995).

[38] A.S. Kheifets and M. Vos, J. Phys. C **7**, 3895 (1995).

[39] E. Weigold and I.E. McCarthy, Adv. Atom. Mol. Phys. **14**, 127 (1978).

[40] L.J. Allen, I.E. McCarthy, V.W. Maslen and C.J. Rossouw, Aust. J. Phys.

43, 453 (1990).

[41] S. Canney, M.J. Brunger, I.E. McCarthy, P.J. Storer, S. Utteridge, M. Vos and E. Weigold, J. Electron Spectrosc. Relat. Phenom. (in press).

[42] N. Ishigure, C. Mori and T. Watanabe, J. Phys. Soc. Japan **44**, 1196 (1978).

[43] J.C. Fuggle, L.M. Watson and D.J. Fabian, Surf. Sci. **49**, 61 (1975).

[44] D.T. Quinto and W.D. Robertson, Surf. Sci. **27**, 645 (1971).

[45] M. Vos and M. Bottema, Phys. Rev. B54, 5964 (1996).

Caption

Fig. 1. The unit cell of α-Al$_2$O$_3$. The z-axis is indicated.

Fig. 2. (a) the valence band structure in α-Al$_2$O$_3$ along the ΓX and ΓZ directions, and (b) the Brillouin zone of the α-Al$_2$O$_3$ crystal.

Fig. 3. The band energies and momentum densities for the upper valence band (two top rows) and the lower valence band (two bottom rows) in α-Al$_2$O$_3$. Highlighted are the total momentum density (momentum density plots) and the band which contributes most significantly to the momentum density (band energy plots). The momenta are in atomic units.

Fig. 4. The schematic representation of the non-coplanar asymmetric geometry used in the (e. 2e) measurements. (a) the scattering geometry. With this geometry the momenta of the target electrons are detected nominally along the y-axis.; (b) the incident and outgoing beams relative to the sample. Shaded area is the exit surface where most detectable (e, 2e) events occur. This determines the surface sensitive nature of the experiment.

Fig. 5. The Auger electron spectra for the evaporated aluminum sample (a) and (c); and the oxidized alumium sample (b) and (d). The Auger LMM peak of aluminum at 69 eV

shifts 12 eV down to 57 eV after the oxidation as shown in (a) and (b). This indicates the formation of the aluminum oxide (Al$_2$O$_3$) layer on the aluminum surface.

Fig. 6. The spectral momentum density plots as measured with the spectrometer for the self-supporting (left panel) and carbon-film-supported (right panel) aluminum oxide samples compared with a LMTO calculation on spherically averaged α-Al$_2$O$_3$ (central panel), respectively. The binding energy is relative to the vacuum level. The highest density in each panel has been normalized to unity. The linear grey scale is shown on the right hand side.

Fig. 7. The measured binding energy spectrum summed over momentum from -2.5 a.u. to + 2.5 a.u. for the self-supporting sample (solid circle with error bars) and the carbon-film-supported sample (open circle with error bars). The raw data of the self-supporting sample have smaller intensity in the higher binding energy peak (the lower valence band) due to the absence of the carbon plasmon energy loss contributions. The solid curve represents the spectrum after deconvoluting plasmon excitations from the raw data of the carbon-film-supported sample. The LMTO calculation (the dashed line) is also presented for comparison. The binding energy is relative to the vacuum level.

Fig. 8. The binding energy spectra from 0.0 a.u. to 1.6 a.u. of momentum at equal intervals of 0.1 a.u.. The raw data (with the error bars) have been deconvoluted for

plasmon excitations (the full line). The dashed curves are results from the LMTO

calculation. The binding energy is relative to the vacuum level.

Fig. 9. The momentum distributions at selected binding energies for the upper valence

band of aluminum oxide. The experimental data are the results after deconvolution of

the raw data for plasmon losses. The dashed curves are results from the LMTO

calculation.

Fig. 10. The momentum distributions at selected binding energies for the lower valence

band of aluminum oxide. The experimental data are the results after deconvolution of

the raw data for plasmon losses. The dashed curves are results from the LMTO

calculation.

TABLE I. Valence band widths in α-Al_2O_3.

Type of calculation	Valence band width (eV)			
	Upper	Gap	Lower	Total
Semi-empirical				
Evarestov et. al [21]	12.06	10.42	5.45	28 23
Ciraci and Batra [19]	11.8	6.3	9 5	27 6
First principles				
Batra [20]	6	10	3	19
Xu and Ching [17]	7.39	8.53	3.26	19 18
Godin and LaFemina [16]	6 5	8.7	3	18 2
Present, LMTO	7.31	8.62	3 39	19 32

Fig. 1: X. Guo et al, Phys. Rev. B

O

Al

O centre of symmetry

z

(a)

Energy (eV)

Z   Γ   X

(b)

Fig. 2: X. Guo et al, Phys. Rev. B

Mom. dens. (a.u.)   Energy (eV)

Upper VB

Γ   X   X

Upper VB

Γ   Y   Γ

Upper VB

Γ   Z   Γ

Mom. dens. (a.u.)   Energy (eV)
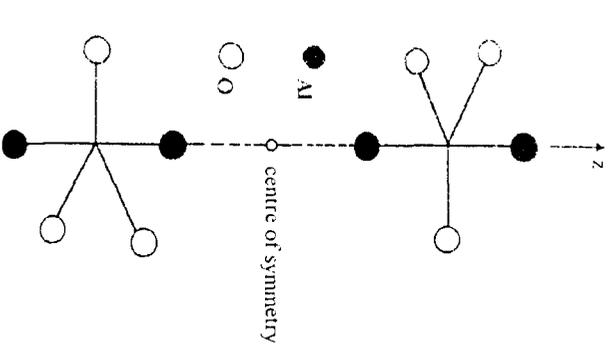
Lower VB
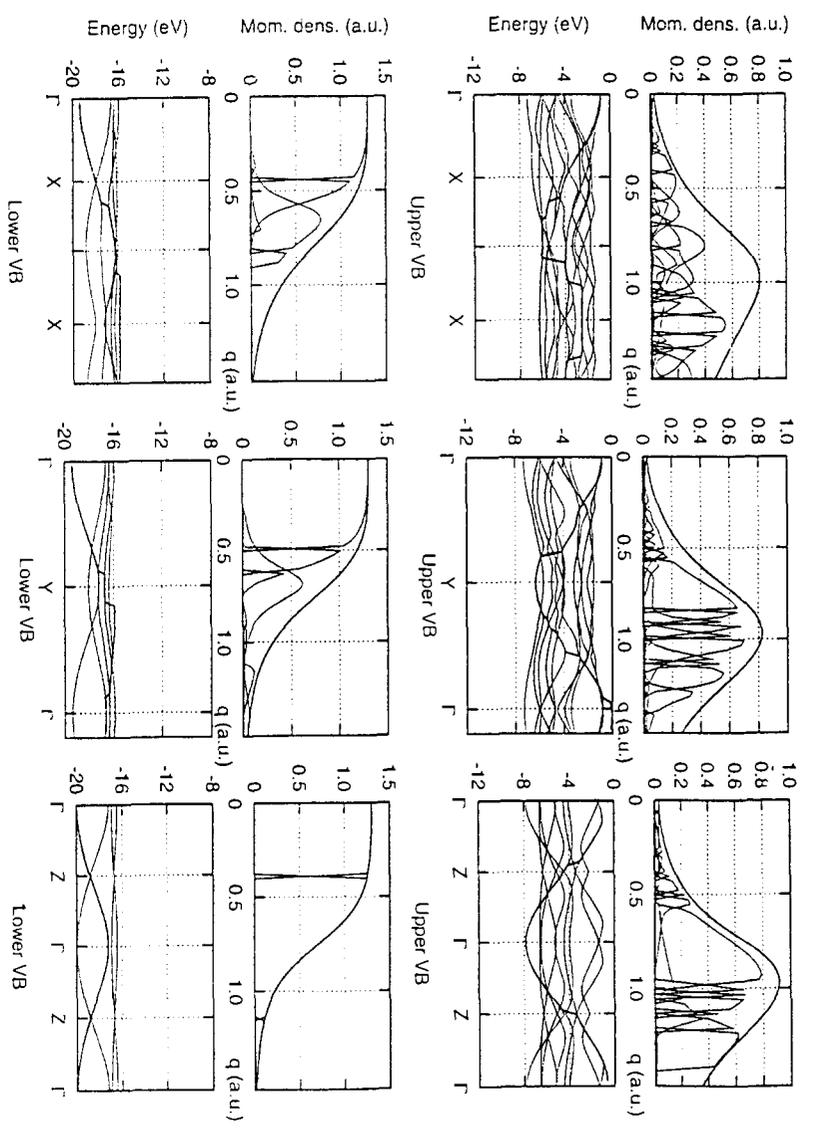
Γ   X   X

Lower VB

Γ   Y   Γ

Lower VB

Γ   Z   Γ
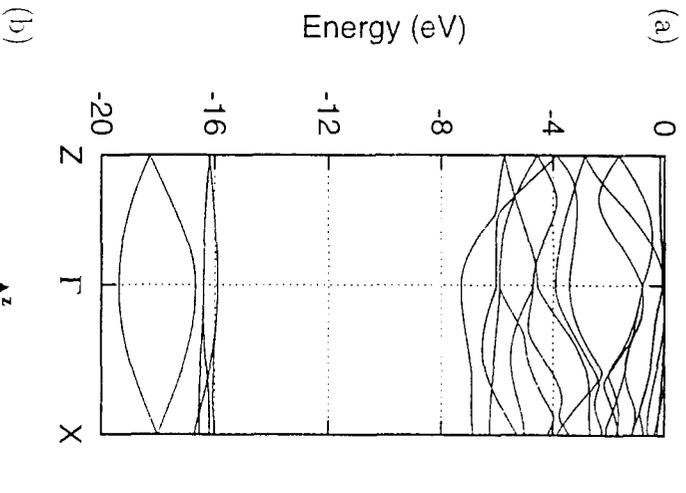
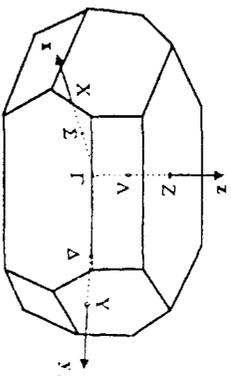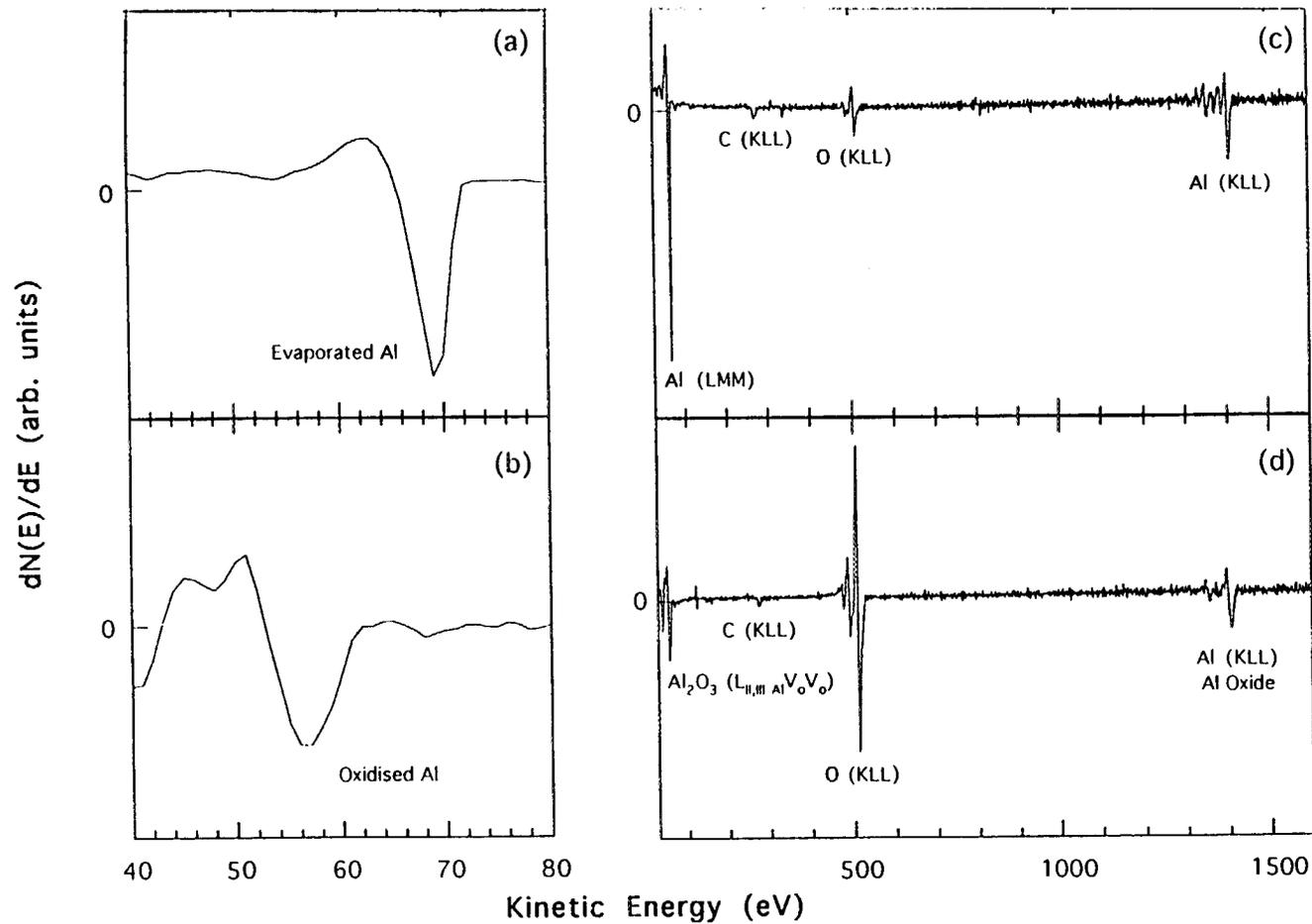Fig. 3: X. Guo et al, Phys. Rev. B

Fig. 4: X. Guo et al, Phys. Rev. B

76° cone

14° cone

(a)

20 keV

30°

n

18.8 keV

14°

76°

1.2 keV

(b)

Fig. 5: X. Guo et al, Phys. Rev. B

(a)

(b) Evaporated Al

Oxidised Al

(c)

C (KLL)

O (KLL)

Al (KLL)

Al (LMM)

(d)

C (KLL)

Al$_2$O$_3$ (L$_{II,III\ Al}$V$_o$V$_o$)

O (KLL)

Al (KLL)
Al Oxide

dN(E)/dE (arb. units)

Kinetic Energy (eV)

(e, 2e) measurement
oxidized 15 nm Al

LMTO calculation
α – Al$_2$O$_3$

(e, 2e) measurement
oxidized 4 nm Al on 5 nm C

Binding Energy (eV)

Momentum (a.u.)

Fig. 6: X. Guo et al, Phys. Rev. B

- Al.-oxide/Polycrystalline Al
- Al.-oxide/Al/a-C
- deconvoluted Al.-oxide/Al/a-C
- LMTO calculation

Intensity (arb. units)

Binding Energy (eV)
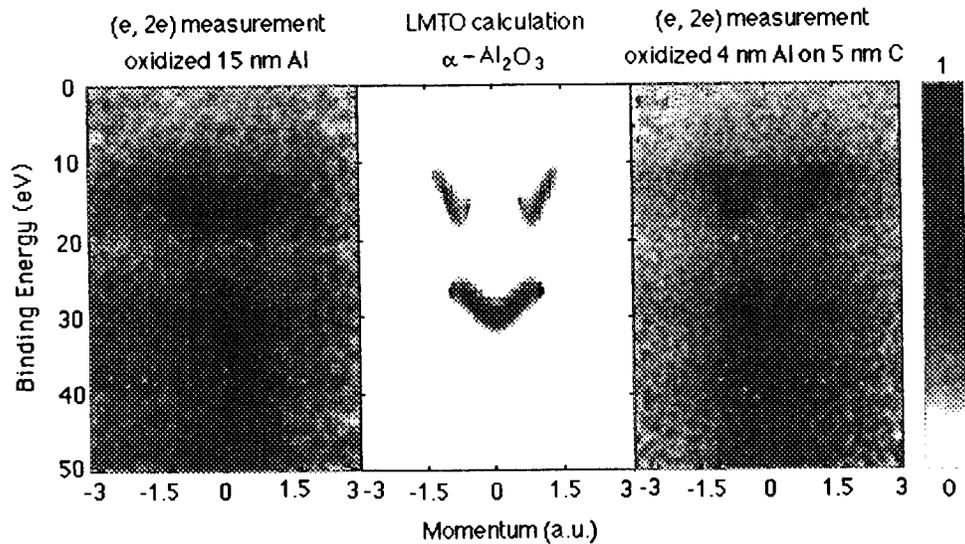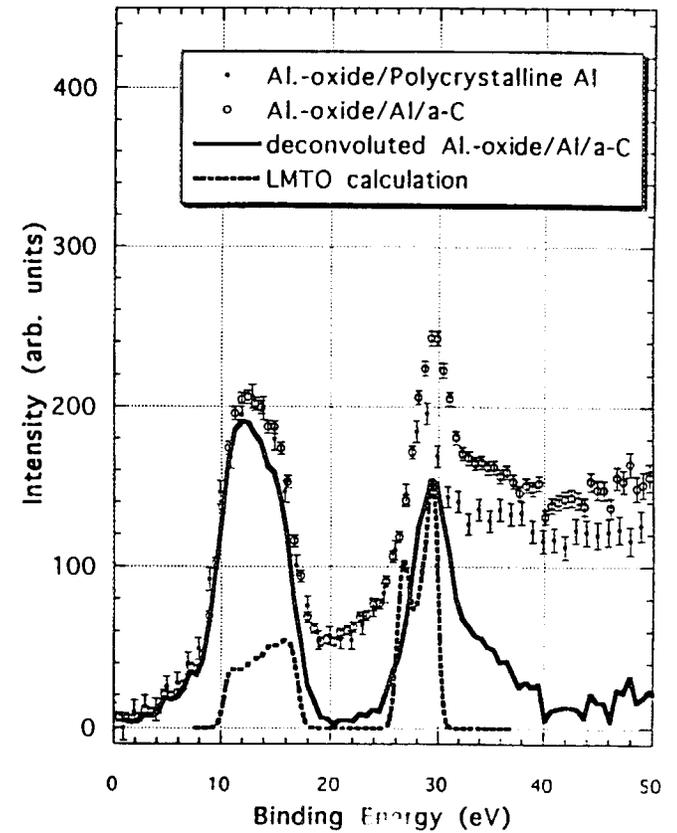
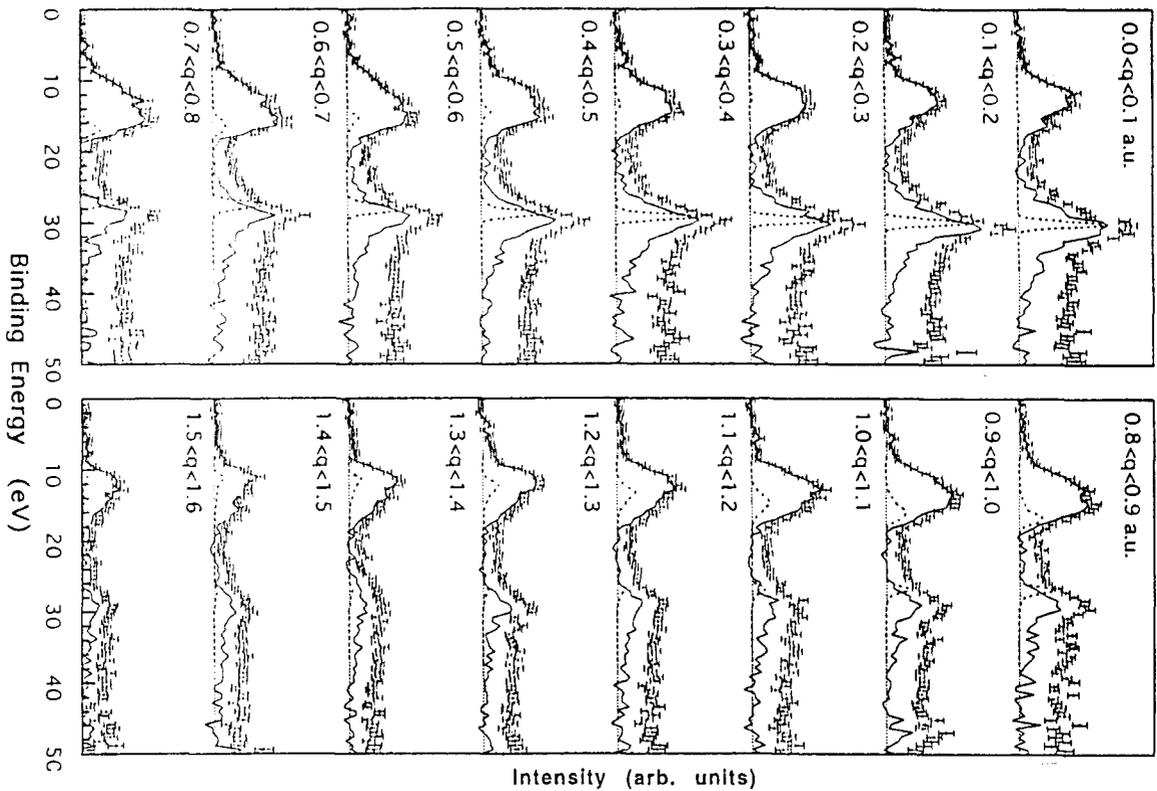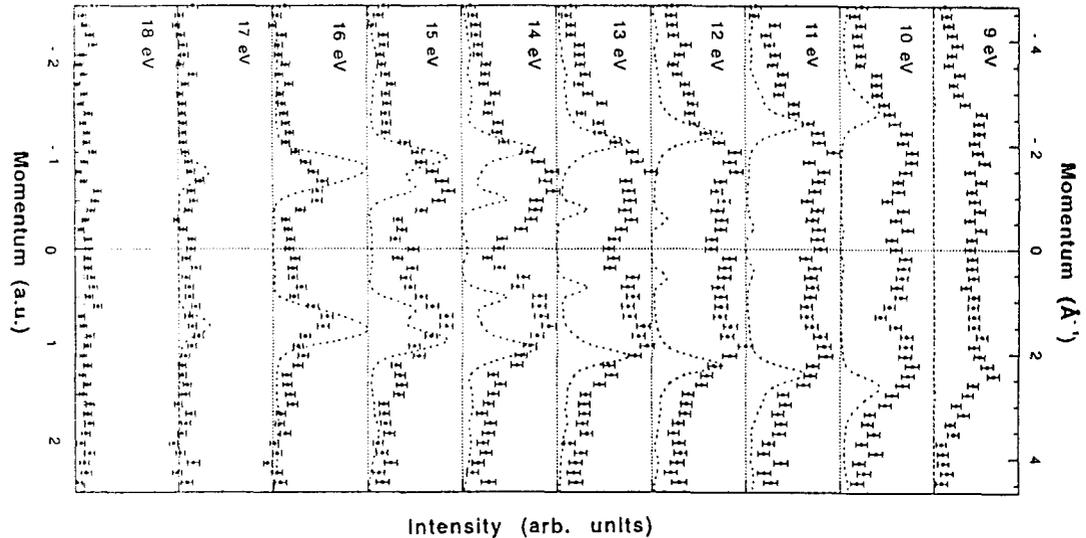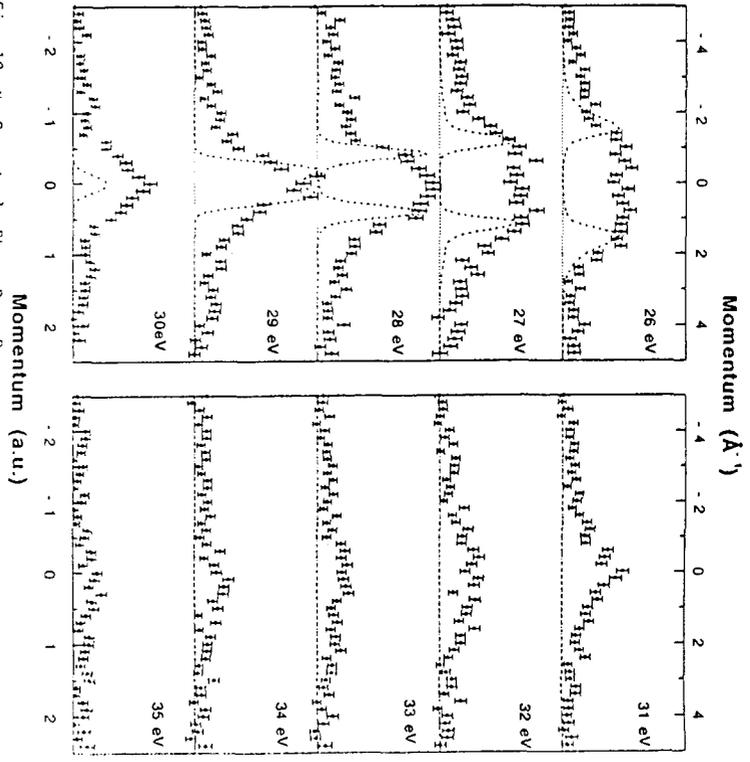Fig. 7: X. Guo et al, Phys. Rev. B

Fig. 8: X. Guo et al, Phys. Rev. B

Fig. 9: X. Guo et al, Phys. Rev. B

Fig. 10: X. Guo et al, Phys. Rev. B